

# Wavelet Analysis of Print Defects

Kevin D. Donohue<sup>†</sup>, Chengwu Cui<sup>‡</sup>, and M. Vijay Venkatesh<sup>†</sup>

<sup>†</sup>University of Kentucky, Lexington, Kentucky

<sup>‡</sup>Lexmark International Inc., Lexington, Kentucky

## Abstract

This paper examines wavelet analyses for detecting and characterizing printing defects. Positive wavelet features for this application include localized space-frequency properties for characterizing defects of limited spatial support (in contrast with the Fourier analysis, which has no spatial localization over the analysis region). In addition, the scale based analyses of wavelets mimic properties of human vision system (HVS) that can be useful for developing thresholds consistent with visual masking and sensitivity. This study examines simulated defects in monochromatic images. Examples illustrate how defects, such as banding, graininess, and streaking appear in the wavelet domain. Wavelet statistics for characterizing printing defects are suggested and their performance tested through Monte Carlo simulations. Simulation results compare the performance of several popular wavelet kernels, such as Daubechies, symlets, and biorthogonal splines. The influence of wavelet properties, such as smoothness and symmetry, on performance is discussed. Detection and estimation results of defects in noise show that symlets generally perform well for characterizing all defects considered. While all wavelets performed well for the banding defects, the biorthogonal spline wavelets performed significantly worse for estimating graininess defect properties.

## Introduction

Useful characterizations for printing defects should mimic the way the human visual system (HVS) senses and perceives these defects. Frequency domain models using Fourier methods have been used because HVS properties have been primarily described in the frequency domain, and the computational properties of Fourier methods are efficient and reliable.<sup>1-4</sup> When an observer evaluates a print sample, he or she compares prints and focuses on known defect patterns. This is a complex process, involving many levels of neural and cognitive processing, that is difficult to model directly. As a result, limitations of the Fourier based models to predict the human perception of printing defects have been observed.<sup>4</sup> Therefore to explore other potential ways to characterize printing defects, this paper considers an alternative approach using wavelets. Wavelet transforms have similar properties to that of Fourier methods, in that spatial signals can be decomposed into frequency bands analogous to the HVS, and efficient computational

structures exist for many wavelets.<sup>5</sup> An advantage of the wavelet approach is that several choices of the transform kernel exist, which may allow for more efficient defect detection, and consequently provide more insight into an individual's image quality evaluation process.

As a first step for applying wavelets to printing defects, this paper compares the ability of different wavelet types to efficiently characterize common defects such as banding, graininess, and streaking. It is often not clear which statistics to apply to characterize the wavelet coefficients of a given signal. Therefore, this initial study also proposes several wavelet statistics for characterizing printing defects and examines their performance with a Monte Carlo simulation. The wavelets considered are limited to discrete orthogonal or biorthogonal types, which are computationally efficient. Continuous wavelets have a greater potential to match the dynamics underlying the defect appearance; however the choices for scaling and translating the wavelet are infinite, and reconstruction kernels to obtain the original signal may not exist, significantly limiting its flexibility.

The Fourier approach for modeling defects has been described in several publications.<sup>1-4</sup> A characterization for the graininess defect is the noise power spectrum (NPS).<sup>2</sup> The NPS shows a linear spectral pattern on a log scale that is characterized by its spectral slope.<sup>3</sup> Streaking also has been modeled in this way, except a steeper spectral slope exists in one of the orientations. The primary characterization for banding has been the FFT of the one-dimensional signal created from either averaging the two-dimensional signal orthogonal to the banding, or averaging the FFTs amplitudes from signal segments. The harmonic amplitudes of the periodic banding structure are used to characterize the banding pattern.<sup>1,4</sup> Statistics analogous to those used on the FFT coefficients and NPS values are examined for wavelet coefficients.

## Wavelet Characterizations

All wavelet decompositions considered in this study can be implemented with a finite impulse response filter (FIR) structure. For a given 2-dimensional signal  $y(n,m)$ , the wavelet decomposition from level  $l$  to level  $l+1$  is given by:

$$y_{uv}^{(l+1)}(n,m) = \sum_i \sum_j y_{11}^{(l)}(2n-i, 2m-j) K_{uv}(i,j), \quad (1)$$

where level 0 is the original signal and the wavelet kernel,  $K_{uv}$ , is composed of 4 different combinations of high and

low-pass filters applied in vertical and horizontal orientations. The subscripts on  $y$  indicate the orientation of its wavelet kernel. Let the wavelet function (high-pass filter) be denoted by  $h(i)$  and the scaling function (low-pass filter) be denoted by  $g(i)$ . Then a class of separable kernels in 2 dimensions for the wavelet decomposition can be defined as:

$$\begin{aligned} K_{11}(i, j) &= g(i)g(j), & K_{12}(i, j) &= h(i)g(j), \\ K_{21}(i, j) &= g(i)h(j), & K_{22}(i, j) &= h(i)h(j). \end{aligned} \quad (2)$$

Subscript 11 refers to the low-pass filter in both the vertical and horizontal directions. In going from one level to the next,  $y_{11}$  from the previous level is used, as indicated in Eq. (1). The scaling by 2 of the arguments of  $y_{11}$  denotes a dyadic subsampling that occurs in going from one level to the next. The levels represent octave subbands, since subsampling scales down the frequency axis of the wavelet kernel by a factor of 2, thereby reducing its effective cutoff frequencies without changing the coefficients. Wavelet decompositions of printing defects are presented in Figs. 1 through 3. Each defect was exaggerated to clearly demonstrate its signature in the wavelet domain.

Figure 1 (a) shows an image degraded by banding. The banding profile was taken from a measured pattern presented in Cui et. al.<sup>4</sup> The banding was applied additively by scaling the banding pattern to 10% of the pixel value in the original image. This resulted in a 20 dB image-to-banding power ratio throughout the image. The wavelet kernel used in this example was the biorthogonal spline wavelet of order 4 on decomposition and 4 on reconstruction.<sup>5</sup> The 2-level wavelet decomposition matrix is shown in Fig. 1 (b), where the coefficients in this figure are presented as the log of their absolute values. The decomposition matrix containing the wavelet coefficients at 2 levels is the same size as the original image due to the subsampling. The  $y_{11}$  output is always placed in the upper left of the wavelet decomposition matrix while, the outputs from kernels  $K_{12}$ ,  $K_{21}$ , and  $K_{22}$  are placed in the upper right, lower left, and lower right, respectively. For each level of decomposition, this is repeated and the  $y_{11}$  region replaced to result in the pattern seen in Fig. 1 (b).

The banding defect signal exhibits low frequency content in the horizontal direction and high frequency content in the vertical direction, which matches the  $K_{12}$  kernel properties. Filter outputs from these kernels are placed horizontally in the 2-level wavelet decomposition matrix. As shown in Fig. 1 (b) the horizontally-placed wavelet coefficients in the decomposition matrix strongly respond to the horizontal lines of the banding defect, while coefficients placed diagonally and vertically exhibit no observable response to the banding defect. The  $K_{12}$  kernel captures energy directly related the high contrast horizontal edges. A Fourier decomposition would also respond to this periodic edge structure, however the energy would be spread out over many coefficients.<sup>4</sup> The wavelet coefficients shown in Fig. 1 (b) capture the edge features with a small set of very localized coefficients. On the other hand,

wavelet coefficients from sinusoidal banding would not be well localized, since the sinusoid is much smoother than the wavelet kernels. For a sinusoid pattern the Fourier decomposition would result in the most localized coefficients. The wavelet coefficient response on banding edges suggests that metrics based on these coefficients may have a potential to respond to defects as the HVS does, since it was shown<sup>4</sup> that the threshold for visually detecting banding was lower for patterns with sharp transitions (like a square wave) than for the sine wave patterns of equal amplitudes.

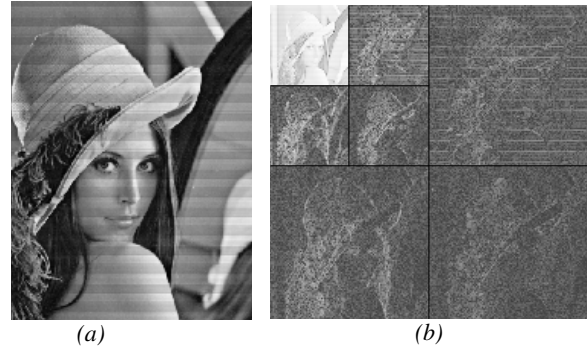


Figure 1. (a) Banding defect, (b) 2-level Biorthogonal spline wavelet decomposition

Figure 2 (a) shows an image degraded by graininess artifacts. The graininess pattern was simulated by passing white Gaussian noise through a filter with a spectrum similar to what has been reported for measured data.<sup>2</sup> A spectrum with a linear roll-off (on a log-linear scale) in both the horizontal and vertical direction was used with a negative slope of -0.17 dB/(cycles/mm). In general, the grain patterns are readily observed in the low frequency regions of the image and are masked in the high-frequency texture regions. In this image, however, the grain modulation at 10% is so strong that it shows up in almost all regions and masks details in the hat, hair, and feather texture regions, and reduces contrast overall. A 3-level wavelet decomposition was performed with an 8<sup>th</sup> order Daubechies wavelet. The wavelet decomposition shows the presence of the graininess energy at every level. The first level decompositions shown in Fig. 1 (b) compared to that in Fig. 2 (b) shows the edge features in Fig. 1 have relatively high coefficient values while those corresponding to the flat fields have low values. Figure 2, on the other hand, shows the corresponding flat fields filled with graininess energy. The intensity values of the graininess energy follow the intensity values of the original image. This occurs because the scaling of the noise process was added to each pixel in the original image based on a percentage of the original image intensity. The random patterns with properties similar to that of graininess have been shown to be efficiently characterized by orthonormal wavelets,<sup>6</sup> therefore suggesting that wavelets may be a more efficient way to represent the graininess defects.

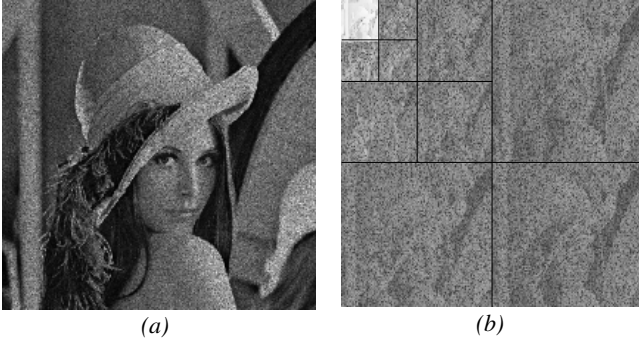


Figure 2. (a) Graininess defect, (b) 3-level Daubechies wavelet decomposition

Figure 3 (a) shows an example of streaking artifacts. This was generated as the graininess artifacts were, except that the spectral roll-off was much faster for the vertical direction (-13 dB/Hz in vertical and -0.87 dB/Hz in the horizontal direction). Thus the streaking artifacts are composed of random features with more low frequency content in the vertical direction and high frequency content in the horizontal direction. This spectral pattern matches the  $K_{21}$  kernel and is consistent with observations in Fig. 3 (b), where significantly more energy exists in the vertically placed wavelet coefficients at all levels.

Based on these general observations of the print defects in the wavelet domain, several statistical metrics can be proposed for detecting and characterizing these defects. Since banding is a periodic phenomenon, statistics such as the autocorrelation function or the FFT can be applied to estimate the periodicity of the banding. The detection of a periodic banding process can be based on the magnitude or a series of related magnitudes in the autocorrelation or FFT. The strength of the banding and its likelihood of being observed can be related to the strength of the actual wavelet coefficients. For the purpose of illustration, this study considered a 3-level wavelet decomposition and reconstructed an image out of equally-weighted horizontal wavelet outputs, excluding  $y_{11}$ . All other wavelet coefficients are set to zero. The reconstructed image is given by:

$$y_{11}^{(l-1)}(n, m) = \sum_{u=1}^2 \sum_{v=1}^2 \sum_i \sum_j w_{uv}^{(l)} y_{uv}^{(l)}(n-i/2, m-j/2) L_{uv}(i, j), \quad (3)$$

where Eq. (3) is applied recursively starting from the highest level to level zero. The weights corresponding to the HVS response are given by  $w_{uv}$ , and the reconstruction kernel (analogous to the decomposition kernels in Eq. (2)) is given by  $L_{uv}$ . The kernel indices are scaled down by 2 in the argument of the higher-level wavelet coefficients to indicate an upsampling (zeros are inserted for non-integer indices). The usefulness of this measure will depend on how well the wavelet filters separate out the critical banding features and quantify them in a way directly related to perception. In this

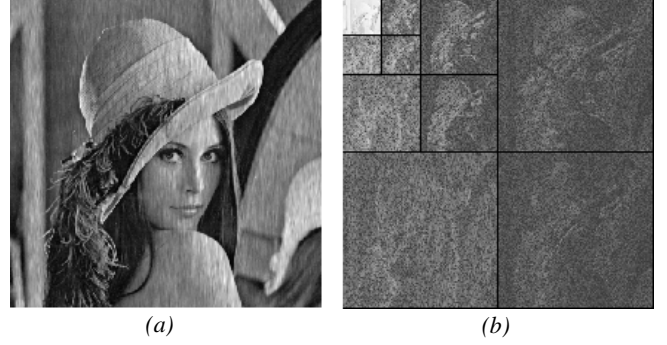


Figure 3. (a) Streaking artifact, (b) 3-level Daubechies wavelet decomposition

example the weights for  $y_{11}$  have been set to 0. This will create problems for the characterization of low frequency banding structures, while the HVS may not be as sensitive to the lower frequency structures, these low frequencies do make a contribution. However, for the sake of illustrating the frequency properties of the wavelet, this high-frequency band weighting system will be used.

The autocorrelation can be applied to the average of the collapsed image along the horizontal direction, given by:

$$A_h(n) = \frac{1}{M} \sum_{m=1}^M Y_k(n, m), \quad (4)$$

where  $Y_h$  is the zero-level image created from Eq. (3). The maximum peak position of the autocorrelation of  $A_h$  can be taken as the banding period estimate. The height of this peak can be used to detect a periodic component. The banding strength can be taken as the maximum peak to minimum peak of  $A_h$  within the period, and is given by:

$$P = \max[A_h(n)] - \min[A_h(n)], \quad (5)$$

where  $n$  is within one period of the detected maximum. The  $P$  value quantifies the power level of the maximum contrast banding defect. Its correlation with human perception will depend on the choice of  $w_{uv}$  in Eq. (3). Examples of  $A_h$  and its autocorrelation for the banding process in Fig. 1 are presented in Fig. 4. The  $A_h$  in Fig. 4 (a) shows the high frequency components of the banding defect. Much of the original image energy was filtered out (into  $y_{11}$ ) and reduced through the collapsed average. The autocorrelation in Fig. 4 (b) shows a strong periodicity at 3.2 mm, which was the period of the banding defect.

Graininess and streaking artifacts have been characterized by the NPS. In particular, the spectral roll-off characterizes the coarseness of the graininess pattern. The steeper the roll-off, the coarser the graininess pattern in the spatial domain. The slope of the spectral roll-off in the horizontal, vertical, and diagonal directions can characterize graininess and streaking defects. This corresponds to the power decrease in the wavelet coefficients in going from the highest level to the lowest level along these directions. Therefore, the slope of the least-squares line fit to the log of

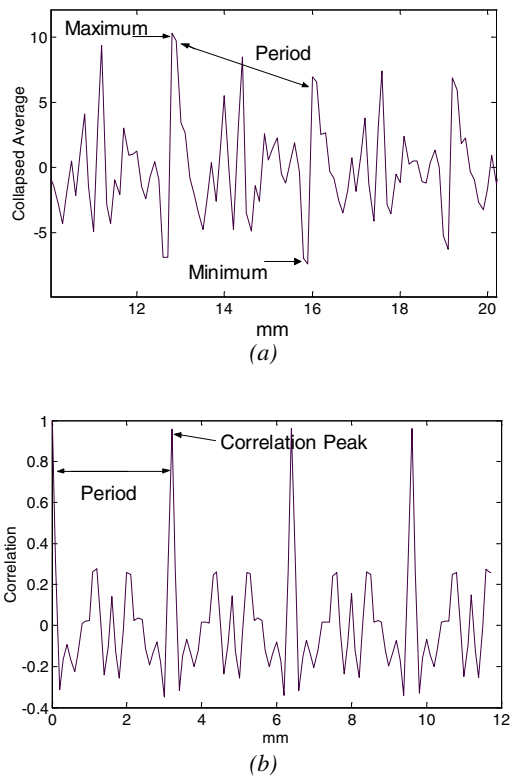


Figure 4 a)  $A_n$  with banding artifact using biorthogonal spline wavelet b) autocorrelation of  $A_n$

the average power at each wavelet level (excluding the  $y_{11}$  power) is used to characterize graininess pattern. Figure 5 shows a line fitted the computed power (denote by the markers) in each wavelet level and orientation on streaking artifacts over a flat field.

The slope of the best-line fit is sensitive to outlier data that may result from actual image structure or other defects present in the print. Therefore, a statistical test should be applied to the region under test to ensure the data is random. In other words, a random pattern should be detected first, before estimating parameters based on this assumption. The entropy or kurtosis is a good statistic for this. In general, random data (white or colored noise) will have high entropy. Low entropy is a sign of structure that may exist in the data. The kurtosis is the ratio of the fourth moment divided by the variance squared. For Gaussian data, the expected value of this ratio is 3. Therefore deviation of the kurtosis from 3 indicates the presence of outliers or structure as in this case. The simulations of the next section will use the kurtosis statistic to describe the randomness of the assumed graininess pattern. If the data cannot be considered random, then the slope has little meaning for the process being analyzed. Using the kurtosis as a detection statistic is analogous to detecting a periodic sequence with the autocorrelation coefficient before attempting to estimate a period.

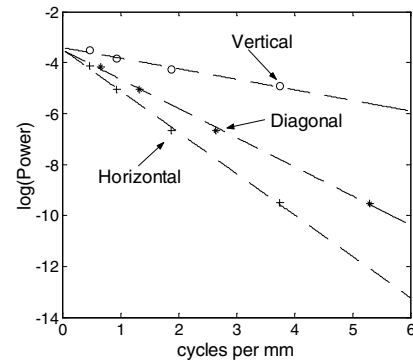


Figure 5. (a) Log power of wavelet coefficients versus the center frequency of wavelet band with least-squares line fit.

## Monte Carlo Simulation

Simulations were performed to test the ability of several different wavelets to efficiently model the print defects. Two general classes of discrete wavelets were applied. One class referred to as orthogonal, includes the Daubechies and symlet wavelets, the other class of wavelets, referred to as Biorthogonal include symmetric wavelets derived from spline functions. The coefficients for the wavelet FIR implementations are shown in Fig. 6. More details about these wavelets can be found in the literature.<sup>5,6</sup> The Daubechies and symlet wavelets have very similar frequency responses, which are characterized as maximally flat; however, neither wavelet is symmetric which is often desired for image processing applications. Symlets are derived to have similar frequency properties as the Daubechies, except that they are as close to symmetric as possible in the space domain. In order to obtain a symmetric waveform and maintain orthogonality, the decomposition and reconstruction kernels must be different. These are referred to as biorthogonal wavelets. The 4 biorthogonal wavelets shown in Fig. 6 are derived from spline functions. The 4 were selected for this study to have 2 anti-symmetric wavelets Fig. 6 (e) and (f), and 2 symmetric wavelets, shown in Figs. 6 (g) and (h). The wavelet order is given in terms of 2 numbers, where the first number is the order of the decomposition wavelet and the second number is the order of the reconstruction wavelet. An increase in order implies more coefficients, which results in a smoother spatial function with greater localization in the frequency domain.

Banding defect patterns were added to flat fields and white noise fields using a square, sine, and a measured banding waveform<sup>4</sup> at 0, .1, 1, and 10% of the original image pixel value. In order to study the performance of the wavelet characterization in noise, no quantization was applied to the simulated images. Clearly, 8-bit quantization would add a level of noise 4 times greater than .1% level at the highest pixel value, and would become a significant

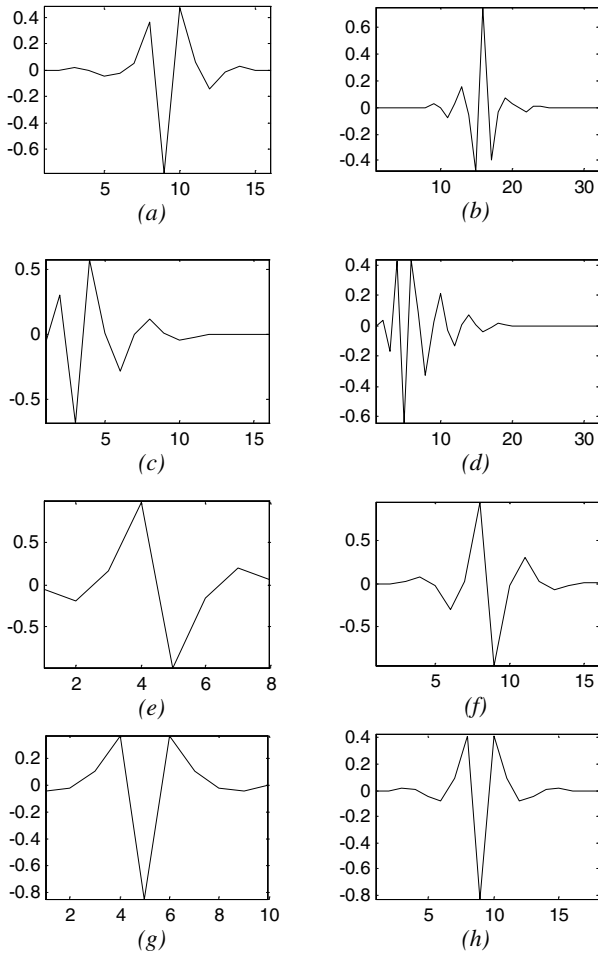


Figure 6: Wavelet functions for the symlet (a) 8<sup>th</sup> order (b) 16<sup>th</sup> order, Daubechies (c) 8<sup>th</sup> order (d) 16<sup>th</sup> order, spline with anti-symmetry (e) order 3.3, (f) order 3.7, Spline with even symmetry (g) order 4.4 (h) order 6.8.

influence on performance. In order to focus on the potential wavelet performance, quantization was not performed. For each estimate in the Monte Carlo simulation, the banding pattern was applied with a random phase and an additive white noise component of  $-60$  dB (the noise variance is equal to the amplitude of the 0.1 % banding). The 0% modulation (just additive noise) represented the baseline for determining detection statistic performance. The  $A_n$  was computed in each run, from which the autocorrelation was computed to obtain the peak value for the banding period estimate. The banding strength measure  $P$  was also computed. This was performed 8 times using the flat field and 8 times with the white noise field.

For the detection of a square wave periodicity using the peak autocorrelation value, most wavelets performed extremely well for the flat field image with over 8 standard deviations (sd) of separation between the 0.1% and 0% banding. In the white noise field the 0.1 % banding was not detectable for any wavelet; however the 1% banding was

detectable with a 2 sd separation in the worst case. The best wavelets in the white noise field were the 16<sup>th</sup> order symlets and the 3.3 biorthogonal wavelets resulting in a 5 sd separation or greater from the baseline. The true period was estimated with 100% accuracy for all wavelets where a period was detected. In terms of the estimated banding strength  $P$ , all wavelets accurately measured these values except for the 0.1% banding in the white noise field. If image energy was normalized, the  $P$  should equal the percent modulation of the banding. In most cases it was slightly less than this because of the loss of banding energy in the  $y_{11}$  wavelet coefficients, which were not used in the reconstruction statistics. In terms of relative performance, the 3.3 biorthogonal wavelet proved the most accurate estimate of  $P$ .

For the detection of the sine wave banding, only the biorthogonal 3.3 and biorthogonal 4.4 wavelets were able to detect this periodicity for all modulation levels (greater than a 5 sd separation between the 0.1 and 0% banding). And in the white noise field only the 3.3 order biorthogonal wavelet was able to detect the 1% banding. In the flat field the 3.3 order biorthogonal wavelet detected the correct period in all cases. In the white noise field, it tended to pick up a sub (half) period peak for the period estimate. Both 3.3 and 4.4 order biorthogonal wavelets had the most accurate  $P$  estimate; however the 4.4 order wavelet did not respond to the 1% banding in the white noise field and neither wavelet responded to the 0.1% banding. Overall the  $P$  estimate was not close to the percent banding because the sine wave's energy was highly localized in the low frequency  $y_{11}$  region, which was excluded from  $A_n$ .

The banding for the measured waveform was detectable by all wavelets with over a 21 sd separation in the worst flat field case. In the white field, the 0.1% banding was not detectable for any wavelet; however, for the 1% banding the 16<sup>th</sup> order symlet and the 3.7, 4.4 and 6.8 biorthogonal wavelets did the best with over a 6 sd separation. All wavelets accurately estimated detected periods, and  $P$  estimates were consistent with square wave results.

The graininess and streaking simulations generated patterns as shown in Figs. 2 and 3 and added them on a flat field with  $-60$ db additive noise. For each estimate, 8 independent (graininess and noise patterns) runs were made in the Monte Carlo simulation. Graininess patterns scaled by 0, .1, 1, and 10% of the original pixel values were added to the original images. To simulate the effects of structure (non random features) on the estimated graininess parameters, estimates from 8 additional runs were performed with a 1% square wave added to the flat field. The first graininess pattern used a slope of  $-0.17$  dB/(cycles/mm) as approximated from the graininess measurements<sup>2</sup> in both the horizontal and vertical directions. The symlets and Daubechies wavelets both did a good job of estimating the actual slope of the graininess pattern in all directions for the 10% and 1% graininess patterns, as predicted by other results.<sup>6</sup> For the 0.1% graininess, the additive white noise biased the estimated toward 0 by about 10%. The biorthogonal wavelets did not perform well. The anti-

symmetric wavelets could not discriminate between white noise and the graininess pattern even for the 10% modulation, and the other 2 biorthogonal wavelets were strongly biased toward zero with high variability overall. When structure was added with the 1% horizontal banding pattern, the symlets and Daubechies wavelets consistently estimated the slopes in the vertical and diagonal directions with good accuracy. The slopes in horizontal direction were strongly biased from the energy distribution in the square wave banding; however, for the 10% graininess pattern the values were only biased by about 10%, indicating that that graininess pattern significantly degraded the 1% structure.

To detect a graininess pattern without structure (to get reliable estimates) the kurtosis of the wavelet coefficients was computed. When no structure was present, for all levels of graininess patterns the kurtosis values and their standard deviations were within .08 of 3, which clearly indicates random Gaussian data. When the horizontal structure was present with no graininess modulation (just additive noise), kurtosis for the horizontal wavelet coefficients was 1.4 points away from 3 with a standard deviation on the order of .05 (i.e. 26 sd separation). As the graininess noise level was increased the kurtosis became closer to 3; however even for the 10% graininess pattern, it was still 1 sd away from 3.

Similar simulations were run for streaking where the slope of the horizontal direction was set at -0.17 dB/(cycles/mm) but the vertical direction was set at -0.86 dB/(cycles/mm). A similar trend was observed as in the first simulation, except that the oval shape of the equi-power level of the NPS created a biasing on the vertical and horizontal estimates. For the vertical estimates from the symlet and Daubechies wavelets, the slope estimates were biased high by about 15% and the horizontal slope estimates were biased low by about 400% (strongly influenced by the low power in the vertical direction). The diagonal estimate was between the horizontal and vertical estimates, but much closer to the horizontal estimate due to the greater power in this direction.

## Conclusions

The observed results for the banding defects indicate that the symlets performed consistently better over all 3 banding waveforms. The difficulty in estimating parameters related to the sine waveform was primarily due to the superior frequency localization of the Daubechies and symlet wavelets. The sine waveform, being highly localized in the frequency domain, had most of its energy in the  $y_{11}$  set of coefficients. This is why the low-order biorthogonal wavelets did the best on the sine wave, since they have the less frequency localization. The square wave and measured waveform parameters were estimated very consistently by the symlet and Daubechies wavelet, indicating that a significant portion of its energy was not frequency localized. While the biorthogonal wavelets did well for the sine wave, they were not as consistent for the square and measured waveform. For graininess noise the choice is clearly between the symlets or Daubechies wavelets. The

biorthogonal wavelets did not perform well. In the case of graininess, good frequency localization is important to estimate the power in each octave band accurately.

The simulation results suggest that symmetry is a good property for estimating banding defects. The lack of good frequency localization for the biorthogonal wavelets did not appear to impair its performance and even helped in the case of the sine wave banding. However, given the irregular shape of the measured banding profile, finding a wavelet to match the sine wave may not be an important concern. There was not a significant performance difference between the orders of the wavelets used in the simulation. In earlier simulations (not reported here), very low-order wavelets did not perform well. At an order of 4 or greater for the symlet and Daubechies began to perform well. If the order was too great, where the number of coefficients began to approach the period of the banding profile, significant errors began to occur in the banding period estimates. Therefore, the near symmetry as in the case of the symlet with sufficient smoothness was shown to be the best all around performer for print defect characterization. The good numerical performance of these wavelets would suggest a next level of work to compare these statistics for various wavelets with results from subjective studies.

## References

1. John C. Briggs, Mike Murphy and Yichuan Pan, "Banding Characterization for Inkjet Printing", IS&T, Portland, OR, 2000, pg. 84-88.
2. Paul J. Kane, Theodore F. Bouk, Peter D. Burns and Andrew D. Thompson, "Quantification of Banding, Streaking and Grain in Flat Field Images", IS&T, Portland, OR, 2000, pg. 79-83.
3. Howard Mizes, Nancy Goodman and Paul Butterfield, "The Perceptibility of Random Streaking", IS&T, Portland, OR, 2000, pg. 89-93.
4. Chengwu Cui, Dingcai Cao and Shaun Love, "Measuring Visual Threshold of Inkjet Banding", IS&T, Montreal, Canada, 2001, pg. 84-89.
5. Gilbert Strang and Troung Nguyen, *Wavelets and Filter Banks*, Wellesley-Cambridge Press, Wellesley, MA, 1996, pg 144.
6. Gregory W. Wornell, *Signal Processing with Fractals, a Wavelet-Based Approach*, Prentice-Hall, Upper Saddle River, NJ, 1996, pg. 60.

## Biography

Kevin Donohue received the B.A. degree in mathematics from Northeastern Illinois University in 1981 and the B.S., M.S., and Ph.D. degrees in electrical engineering from Illinois Institute of Technology in 1983, 1984, and 1987, respectively. He is currently an Associate Professor in the Electrical and Computer Engineering Department at the University of Kentucky. His current research interests include image, audio, and ultrasonic signal processing. He is a member of IEEE and Sigma Xi.